

Sub-Millinewton Thrust Stand and Wireless Power Coupler for Microwave Powered Small Satellite Thrusters

Benjamin N. Wachs* and Benjamin A. Jorns

Department of Aerospace Engineering, University of Michigan, Ann Arbor, Michigan 49109, USA

(Dated: July 13, 2022)

The design and performance of a thrust stand for characterizing low-power electric propulsion thrusters is presented. The thrust stand is capable of sub-millinewton resolution for devices on the order of 1 kg. The architecture is based on a counter-weighted hanging pendulum design, a variant of the standard hanging pendulum that employs a counterweight to increase force resolution. Thrust is measured in a displacement mode using the change in position of the pendulum arm as measured by an optical displacement sensor. Passive eddy-current damping is used to offset oscillations and decrease setting time. An *in-situ* calibration rig using known masses is used to calculate thrust. The thrust stand features an adjustable counterweight for in-vacuum sensitivity adjustment. In addition, the design of a broadband (600-2490 MHz) wireless microwave power coupler is presented. The device eliminates stiffness and thermal drift introduced by coaxial cables – typically the leading source of error in testing low-power microwave and radiofrequency powered thrusters. The thrust stand and coupler were tested using an electron cyclotron resonance magnetic nozzle thruster operating with xenon at flow rates from 1-10 sccm and powers ranging from zero (cold gas thrust) to 40 Watts. The resulting measurements showed a force resolution of $\sim 10 \mu\text{N}$ over a range of thrusts from ~ 14 to $600 \mu\text{N}$.

I. INTRODUCTION

Low-power ($< 500 \text{ W}$) Electric Propulsion (EP) technology has seen a rapid growth in recent years as small satellites have found increasing use in commercial and scientific missions [1, 2]. The high specific impulse provided by EP thrusters (and thus low propellant usage) yields substantial cost savings and enables constellation-type missions that would be prohibitively expensive or difficult with the larger mass and volume footprint used by chemical propulsion. In light of these advantages, there are a number of parallel efforts to develop electric propulsion technologies at this low power level [3].

These development efforts, in turn, typically require direct thrust measurements to evaluate thruster forces, specific impulse, and efficiency. Performing these measurements accurately is fraught with challenges, largely owing to the low thrust-to-weight ratio inherent to EP thrusters [4]. While there exist a variety of proxy methods for determining thrust, e.g. electrostatic probes, laser induced fluorescence measurements, and momentum flux sensors, these procedures rely on several assumptions and are typically untrustworthy for absolute thrust measurements [5–8].

One type of low-power concept where direct performance measurements have proved to be particularly challenging is the microwave-based thruster. This is a technology where microwaves are used to heat or ionize a propellant, and the resulting gas or plasma is expelled through a physical nozzle, magnetic nozzle, or electrostatic grids to produce thrust. Examples of these devices include the electron cyclotron resonance (ECR) magnetic nozzle [5, 9, 10], electrothermal devices [11], and ECR gridded ion thrusters [12]. Thrusters of this variety intended for small satellite applications typically operate at power levels between 10 and 100 W with thrust outputs in the range of 0.1-2 mN. There are several constraints that make thrust measurements of these devices problematic. For example, the low powers tend to generate low force levels, thus requiring higher resolution than higher power EP systems. This problem is compounded by the high levels of electrical and thermal noise produced by these thrusters. Similarly, the relatively large-diameter coaxial microwave cabling used in these systems thermally expands at rates higher than the stranded-wire used in testing DC thrusters. This acts as a major thermal drag that can overwhelm the low levels of thrust generated by the device. Finally, thrust measurement techniques must also be compact enough to fit into the small chambers used in low-power EP testing, and ideally should place the thruster far from conductive walls that can perturb thruster operation [13].

There have been a number of efforts to develop thrust measurement techniques that overcome these challenges for microwave systems at low power [9, 14, 15]. From these efforts, it has become a common practice to employ a wireless power coupler to transmit power from the fixed to the moving parts of the the thrust stand, thus eliminating a major source of thermal expansion. This is typically achieved using a two rectangular waveguides separated by a small air gap [14]. However, this approach is subject to alignment issues as different parts of the thrust stand rotate about each other and can prevent the use of frequencies out of range of the rectangular waveguides. This latter consideration in particular is important as there is growing evidence that varying the frequency of the microwaves may lead to significant performance improvements [16]. To be able to perform a

* Author to whom correspondence should be addressed: bwachs@umich.edu

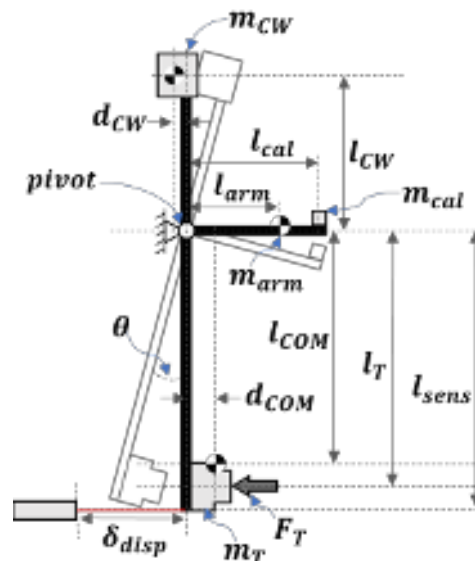


FIG. 1: Schematic of thrust stand showing in null ($\theta = 0$) and displaced orientations.

detailed optimization study of these devices, there is a need for a wireless power coupling scheme for the thrust stand that can accommodate a wider bandwidth of microwave frequencies.

To address this need, we present in this paper the design and performance of a hanging pendulum thrust stand equipped with a novel broadband microwave wireless power coupler. This coupler allows microwave power in the range of 600-2490 MHz to be transferred to the thrust stand. We test thrust stand with an ECR magnetic nozzle thruster as a test article and demonstrate a force sensitivity of $25\mu\text{N}$ with measurement range of 0-0.7 mN. While the emphasis of this paper is microwave-powered thrusters, it should be noted that the thrust stand is compatible with other low-power EP thrusters. This paper is organized as follows: In Sec. II we describe the operating principle of the thrust stand and calculate its predicted performance. Section III details the components used in implementing the thrust stand including the overall dimensions, electronic components, wireless power coupler, calibration systems, and the ECR thruster used in testing. Section IV describes the experimental setup used to characterize the thrust stand. In Sec. V, we present the results of our thrust stand characterization, including calibration, thermal drift, electrostatic interference, and thruster testing. We use these results to generate an uncertainty estimate for our measurements. Finally, we discuss our results in the context of low-power ECR thruster testing in Sec. VI.

II. THRUST STAND OPERATING PRINCIPLE

In this section, we provide an overview of our thrust stand including the basic dynamical model for its operation. Figure 1 shows an illustration of the inverse pendulum type thrust stand with typical values associated with our design listed in Table I. This configuration is similar in layout to thrust stands that have been used previously to characterize ECR thrusters [9, 17] and ion thrusters [18, 19]. The system operates by measuring the change in angular position, θ , with respect to a central pivot point of a pendulum arm that is induced by the force of a thruster, F_T located at a distance l_T , from the pivot. The pivot point is physically implemented using a flexural pivot (a bearingless torsional spring), as described in Sec. III. The displacement is correlated to force readings using a series of mass calibration weights, m_{cal} , located at a distance, l_{cal} , from the pivot. The use of a counterweight, m_{CW} , at a distance l_{CW} , above the pivot point in turn allows for increased sensitivity compared to a conventional hanging pendulum design.

We show in Appendix A that subject to a moment analysis about the pivot point and assuming a small angle approximation, we can formulate an expression for the linear displacement in the horizontal plane of the thrust stand located at the location, l_{sens} , of a displacement sensor:

$$\delta_{disp} = A_T F_T + b_0, \quad (1)$$

where the slope of the line is given by

$$A_T = l_{sens} \frac{l_T}{m_T g l_T - m_{CW} g l_{CW} + k}, \quad (2)$$

where k is the spring constant of the flexural pivot and g is the acceleration of gravity.

TABLE I: Thrust stand properties

	Description	Value	Units
F_T	Thrust force	0.1-1	mN
m_T	Thruster mass	1.5	kg
m_{CW}	Counterweight mass	1.5	kg
m_{cal}	Calibration mass	0.1	g
l_T	y length from pivot to center of thrust	0.305	m
l_{COM}	y length from pivot to thruster center of mass	0.305	m
d_{COM}	x length from pivot to thruster center of mass	0.05	m
l_{CW}	y length from pivot to counterweight center of mass	0.08-0.22	m
d_{CW}	x length from pivot to counterweight center of mass	0.00	m
l_{cal}	length from pivot to calibration weight center of mass	0.102	m
k	Pivot stiffness	0.0016	N-m/degree

From Eq. 2, we note that the sensitivity can be increased (greater change in displacement per unit thrust) by changing the counterweight mass, m_{CW} , or position, l_{CW} . This feature enables us to trade between higher signal to noise ratio (larger $m_{CW}l_{CW}$) and measurement settling time (smaller $m_{CW}l_{CW}$). Given the values shown in Table I, we can estimate the thrust stand's sensitivity to be on the order of $A_T \approx -0.1$ mm/mN.

As the actual values in the expression for the slope may not be directly measurable, in practice we infer A_T by employing a calibration procedure based on applying known weights to the calibration arm. This follows a similar approach to that described in Ref. [17]. We show in Appendix B that the relation between applied calibration mass and displacement is given by

$$\delta_{cal} = A_{cal}(m_{cal}g) + b_{cal}, \quad (3)$$

where A_{cal} is a slope that is different than the slope that results from the application of thrust. This difference stems from the fact that the calibration weights and thrust are applied at different locations in the pendulum. By periodically adding weights to the calibration, we can regress the displacement as a function of mass to find a slope value, A_{cal} . Geometrically, we then can relate relate this calibration slope to the slope in Eq. 1 with the expression:

$$A_{cal} = \frac{l_{cal}}{l_T} A_T \quad (4)$$

where $\frac{l_{cal}}{l_T} = \frac{1}{3}$ in our design. This calibration procedure must be repeated every time the counterweight is adjusted.

In certain cases, it can be important to understand the thrust stand's dynamical response. For instance, when testing pulsed devices, the thrust stand's natural frequency can interact with the excitation frequency generated by the thruster. Furthermore, some missions have strict thruster noise requirements within a certain frequency bands [17], thus requiring a detailed understanding of the frequency spectrum generated by the thruster. While these types of tests are not the focus of this paper, we provide a theoretical overview of the thrust stand's dynamical response in Appendix C. Using a first order pendulum analysis with the dimensions given in Table I, we can calculate the thrust stand's natural oscillation frequency to be $f_0 \approx 0.3$ Hz. Measuring the noise produced by the thruster at frequencies commensurate with or above f_0 requires taking into account the thrust stand's frequency response. More information on this procedure can be found in Ref. [20].

III. PHYSICAL DESCRIPTION

Figure 2 shows a detailed diagram of the thrust stand implemented for this study. This system consists of an aluminum mounting frame connected to an aluminum pendulum arm through two flexural pivots (shown in Fig. 2 D). Our design uses two Riverhawk 5016-800 pivots, each with a 0.0008 N-m/degree stiffness constant and a 26 kg load capacity. Combined, this gives a stiffness of 0.0016 N-m/degree and a total load capacity of 52 kg. The thrust stand uses two motorized counterweights. The vertical counterweight (G) adjusts the thrust stand's sensitivity, as described by l_{CW} in Eq. 2. It consists of a 1.3 kg brass block connected to a pair of motorized lead screws allowing for precise in-vacuum positioning. The horizontal counterweight (A), is used to level the pendulum arm in-vacuum. By positioning the thruster perpendicular to ground, we minimize calibration errors that can result if the gravitational vector is not aligned with the pendulum arm when the calibration starts. It is implemented with an aluminum block that slides across linear guide rails using a pair of PTFE sleeve bearing carriages. The block is connected to a stepper motor via a lead screw giving sub-0.01 mm resolution.

We measure the displacement, δ , using a Philtec D63 fiberoptic sensor, shown in Fig. 2 (C). The sensor measures the intensity of light reflected from a target surface – a gold-coated mirror in our design – to determine the distance from sensor tip to target.

This is the author's peer reviewed, accepted manuscript. However, the online version of record will be different from this version once it has been copyedited and typeset.
PLEASE CITE THIS ARTICLE AS DOI:10.1063/1.5008831

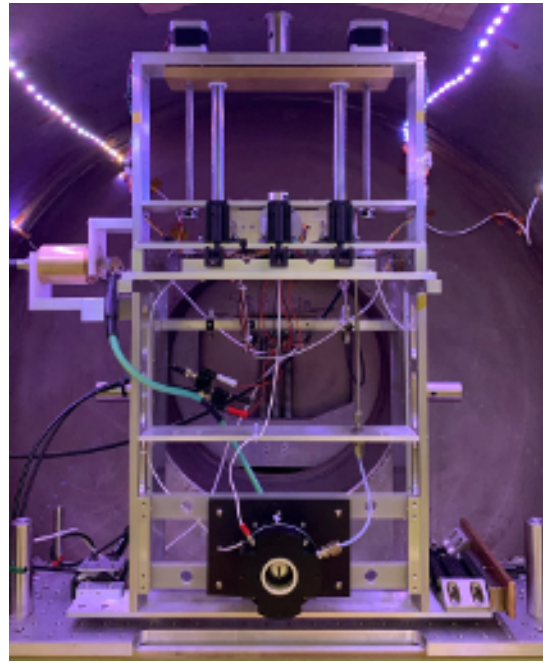
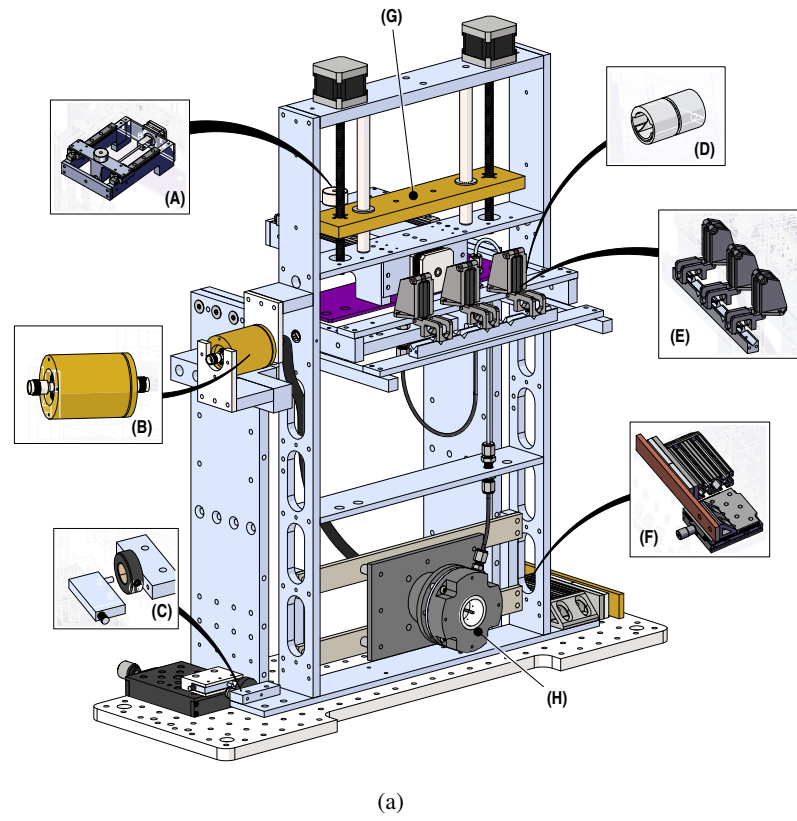


FIG. 2: (a) Thrust stand model showing (A) horizontal counterweight, (B) wireless power coupler, (C) optical displacement sensor, (D) flexural pivot, (E) calibration system, (F) eddy-current damper, (G) vertical counterweight, and (H) ECR thruster, and (b) thrust stand with ECR thruster installed in the Junior Test Facility

The D63 has a sensitivity of $2.7 \text{ mV}/\mu\text{m}$, which translates to a thrust sensitivity on the order of roughly $10 \text{ mN}/\text{mm}$ using Eq. 2. The sensor's light output is fiber-coupled to control electronics (located outside of the vacuum chamber) that provide an analog 0-5 V signal. We read this output using an 18-bit National Instruments PXI-6289 DAQ. We note that while many past thrust stand designs have employed linear variable differential transformer (LVDT) sensors for displacement measurement, optical based sensors have been shown to be more impervious to electric noise emitted by RF thrusters [21].

Our design employs an eddy current damper (Fig. 2 (F)) to reduce oscillations caused by environmental noise and changes in thrust output. The damper consists of neodymium magnets backed by magnetic steel mounted to the bottom of the pendulum arm. A copper bar is mounted to a linear translation stage opposite the permanent magnets. By adjusting the distance between the magnets and the copper, we can modify the thrust stand's damping ratio. The damping ratio dictates the settling time for each thrust measurement, with a critically damped pendulum providing the minimum settling time. Practically, reaching a critical damping ratio can be difficult given the finite magnet strength used in our design. For the results presented in this paper, the distance between magnets and copper is 1 mm, which corresponds to a near-critically damped response. All magnetic materials are kept on the swinging portion of the thrust stand in an effort to prevent net forces from being generated by the interaction of the damper and thruster magnetic fields. This is of particular importance as the thruster's magnetic field strength varies with changes in temperature.

We show a schematic diagram of the thrust stand's electrical and fiber-optic connections in Fig. 3. The thrust stand features two microcontrollers used to communicate with an external DAQ and control on-board sensors and motors. One is attached to the fixed portion of the thrust stand while the second is mounted to the rotating pendulum arm. The fixed microcontroller has two PT100 resistance temperature detectors (RTDs) for measuring the temperatures along the side of the thrust stand frame and the fixed side of the flexural pivots. This microcontroller is also used for controlling the actuators used by the calibration system. The second microcontroller (attached to the swinging pendulum arm) has two PT100 RTDs for measuring the temperatures at the thruster and at the rotating end of the flexural pivots. It also controls an on-board tilt sensor (ADIS16209) and three stepper motors used by the horizontal and vertical counterweight systems. The tilt sensor is not strictly necessary for taking thrust measurements but ensures a consistent starting position for the thruster. The two controllers are connected using a two-wire UART connection. The stationary controller in turn communicates to the external DAQ via a USB feedthrough.

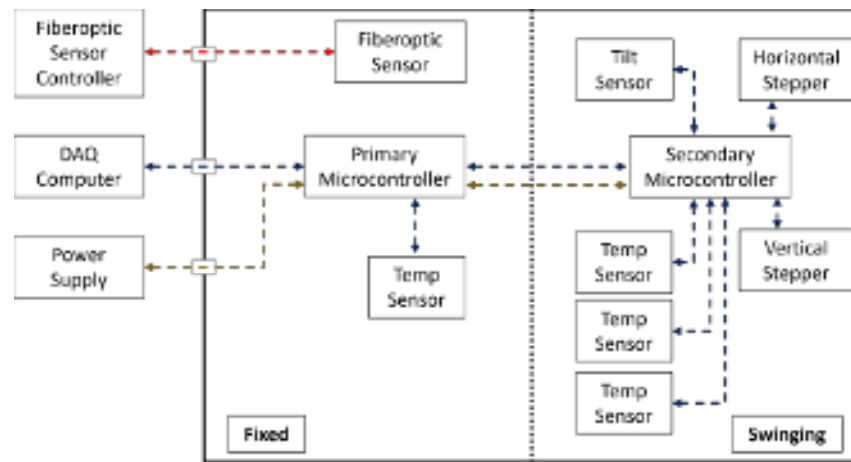


FIG. 3: Schematic diagram of the thrust stand's electrical and fiber-optic connections.

In addition to the above sensors, we include an electrical connection to measure or set the voltage at the thruster body, V_{sense} . The thruster's floating potential can be a useful metric in determining plasma properties [22]. This connection also enables us to test the thrust stand's electrostatic response to determine if the thruster's floating voltage can produce false thrust readings, as shown in Sec. V D.

In total there are five, low-power DC electrical connections between the swinging and fixed portions of the thrust stand to facilitate communications and control. These electrical connections to the swinging portion of the pendulum are made by draping 18 gauge stranded silicone jacketed wire between two screw terminals. This "waterfall" configuration helps relieve strain between the fixed and swinging portions of the thrust stand, thus reducing potential sources of drag or drift from the effects of thermal deformation. The gas interface consists of a 1/4 inch fluoroelastomer tube which is also attached in a waterfall configuration. We transmit microwave power to the thrust stand via a wireless power coupler. As described in the next section, this method reduces a major source of thermal drag on the thrust stand.

A. Wireless Power Coupler

Thermal drifts caused by changes in material stiffness and density are a ubiquitous source of error in thrust stand testing. Of particular concern in EP measurements are the electrical interfaces to the thruster (commonly referred to as the "waterfall"). Testing radiofrequency (RF) and microwave powered thrusters presents a particular challenge as the coaxial cables used to transmit power to the thruster are typically stiffer than DC power lines and contain materials — PTFE or polyethylene — that have relatively high thermal expansion coefficients [23]. Furthermore, because of skin depth and dielectric loss effects, these cables tend to absorb more power during testing than their DC counterparts, further compounding thermal drift errors. While other thrust stands designs have addressed this problem for DC connections by using liquid metal contacts, this solution becomes much more challenging for RF currents when skin depth and impedance matching effects must be considered [24][25].

To avoid thermal drifts and friction associated with coaxial lines, previous thrust stands have featured non-contact methods to transmit microwave power to the pendulum arm. These wireless schemes have included stripline joints [15] as well as narrowly separated rectangular waveguides [13, 26]. This wireless approach has the additional benefit that it acts as a DC isolator, eliminating the need for lossy DC blocks on the thrust stand for tests requiring galvanic isolation between the thruster and thrust stand. While these previous approaches to wireless coupling have been successful, they have two practical limitations. The first is the tight alignment required by planar stripline joints, where small misalignments can lead to reflected power. The second limitation stems from the finite bandwidth associated with rectangular waveguides, which can inhibit tests requiring broadband frequencies.

To overcome these practical challenges with stripline and rectangular waveguides, we employ a wireless power coupler based on a coaxial geometry, shown in Fig. 4. Our coupler uses two axisymmetric, coaxial halves separated by a 1 mm gap. During operation, half of the coupler rotates about the central axis as the thrust stand pivots. Because the design is axisymmetric, we thus are able to maintain the original alignment throughout operation. This largely eliminates challenges associated with varying alignment during operation for striplines and rectangular waveguide designs.

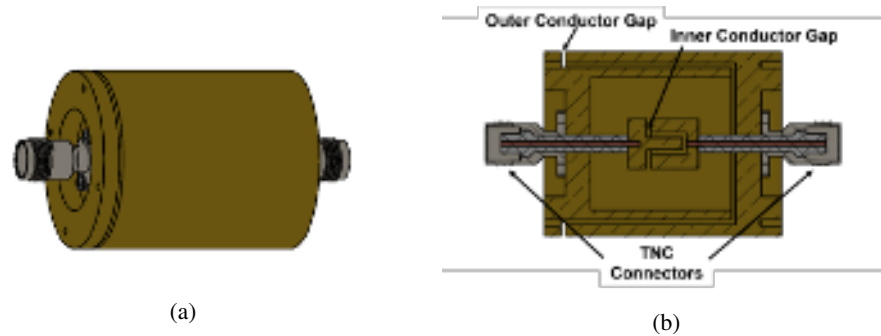


FIG. 4: CAD drawing showing wireless power coupler showing (a) dimetric and (b) cross section views.

As for the bandwidth, each half of the coupler is designed to form a 50Ω air dielectric coaxial line. Power is capacitively coupled across the gap. We use a length of the coupler (~ 5 cm) that corresponds to a quarter wavelength at the middle of our frequency range of interest (1700 MHz). Per Ref. [27], the choice of a quarter wavelength renders the system relatively insensitive to the discontinuities from the air gap, thus reducing reflected power. Fig. 5 shows results for the s-parameters of this coupler generated from simulations with COMSOL multiphysics. These show a -1 dB bandwidth — the range over which 90% of incident power is transmitted — from 800-2600 MHz. Once we constructed the coupler, we performed direct tests on the bandwidth with an Agilent E5071C network analyzer. As shown in Fig. 5, the measurements are approximately consistent with simulation with -1 dB bandwidth from 600-2490 MHz with low ($<10\%$) reflected power over the entire bandwidth. The implication of these results is that this design has a substantially expanded bandwidth compared to rectangular waveguides—thus enabling expanded parametric studies of the impact of microwave frequency.

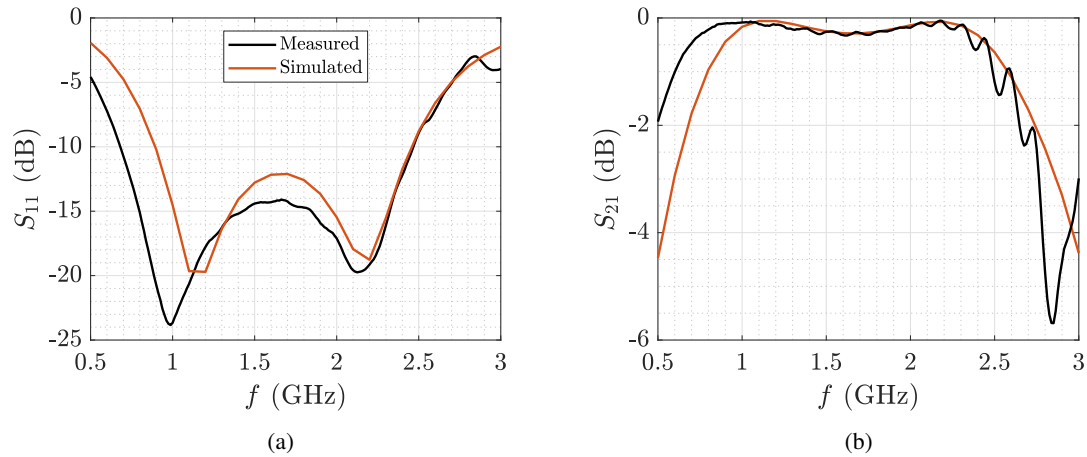


FIG. 5: Wireless power coupler simulated and measured S parameters with (a) reflection coefficient, S_{11} , and (b) transmission coefficient, S_{21} .

B. Calibration System

In Sec. II, we introduced the calibration principle for hanging pendulum thrust stands. We implement this system using a series of servo actuators to drop calibration weights onto a calibration weight catching bar that is mounted to the pendulum. We show a picture of the calibration system in Fig. 6. The calibration weight catching bar is located a distance l_{arm} from the pendulum pivot point, as shown schematically in Fig. 1. The bar features a v-groove to ensure consistent placement during each drop. The weights do not require a string to hold them in place, thus eliminating a common source of error in calibration setups. This is similar to the setup shown in Ref. [17]. Because each actuator operates independently, using two calibration weights can yield three test points while three calibration weights provides six different test masses. The current thrust stand configuration uses two calibration masses weighing 0.0495 and 0.1798 g.



FIG. 6: Calibration mechanism showing servo actuators and the calibration weight catcher bar.

IV. EXPERIMENTAL SETUP

In this section, we detail the experimental setup used in characterizing the operation of the thrust stand. Key elements include the vacuum facility and the ECR thruster.

A. Vacuum Facility

The experiments were conducted in the Junior Test Facility at the University of Michigan Plasmadynamics and Electric Propulsion Laboratory. This vacuum facility is a cylindrical stainless steel clad chamber measuring 1 meter in diameter by 3

meters in length. It is equipped with two high-vacuum pumps: a turbomolecular pump (Leybold Mag 2000) rated for 1550 liters/s on N_2 (~ 1240 liters/s on Xe), and a cryogenic plate capable of pumping roughly 38500 liters/s on xenon. The cryogenic pump maintained a temperature of ~ 30 K throughout testing. The actual pumping speed observed during the experimental campaigns ranged from approximately 19000 to 30000 liters/s xenon. The discrepancy between predicted and measured pumping speeds was likely caused by partial blockages of the cryogenic pumping surface during thruster testing. We measured pressure in the chamber using a Stabil Series 370 Ion Gauge (calibrated for nitrogen) mounted in plane with the thruster. The base pressures were below 10^{-7} Torr- N_2 throughout the duration of the tests. More details on the test facility and pumps are provided in Ref. [28].

B. Thruster

In the experimental campaign, we used a low power ECR magnetic nozzle thruster based on a design from the Office National d'Etudes et de Recherches Aéropatiales (ONERA) [5]. Figure 7 shows a notional illustration of the thruster as well as an image of it running with xenon propellant. Magnetic nozzle thrusters operate by generating and heating a plasma using RF or microwave energy. The resultant plasma produces a net thrust as it is expelled through an expanding magnetic field. These thrusters offer a simple architecture lacking the plasma contacting cathodes and multiple power supplies needed for traditional EP systems. The ECR-type magnetic nozzle thruster uses resonant absorption that occurs where the frequency of the input electromagnetic energy, ω_{RF} , matches the electron gyration frequency about a DC magnetic field line, ω_{ce} . In the test article we employed for our experiment, a coaxial structure excited a TEM wave within the thruster's discharge region. Permanent magnets provided the DC magnetic field needed for both resonance and generating the diverging magnetic nozzle.

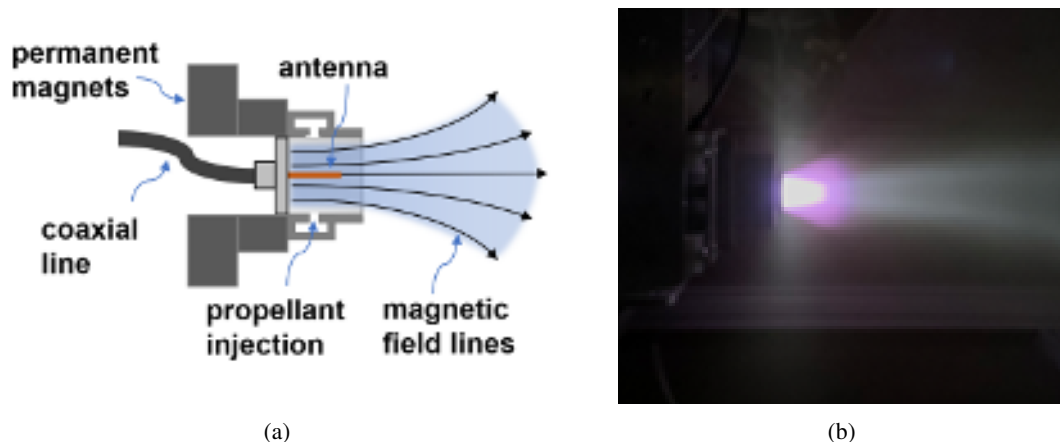


FIG. 7: Schematic view of the (a) ECR thruster and (b) the ECR thruster firing in vacuum.

In our experimental setup, we used a 2.4 GHz microwave waveform as the input power to the thruster. This frequency corresponds to a resonant magnetic field strength of 859 Gauss. The microwave power was generated by a solid-state power amplifier and was read by thermocouple type microwave power sensors (Keysight N8482H) connected to a 20 dB directional coupler which taps the forward and reverse power into the chamber. The thruster was held in an electrically floating configuration with both the thruster body and inner conductor isolated from the thrust stand by means of the wireless power coupler. The thruster was mounted to the thrust stand using a G-10 fiberglass insulator.

V. EXPERIMENTAL RESULTS

In this section, we present the results of a series of experiments characterizing the thrust stand's operation. These were performed with the ECR test article described in the previous section. We quantify in the following the noise, sensitivity, thermal drift, and susceptibility to electrostatic interference of the system.

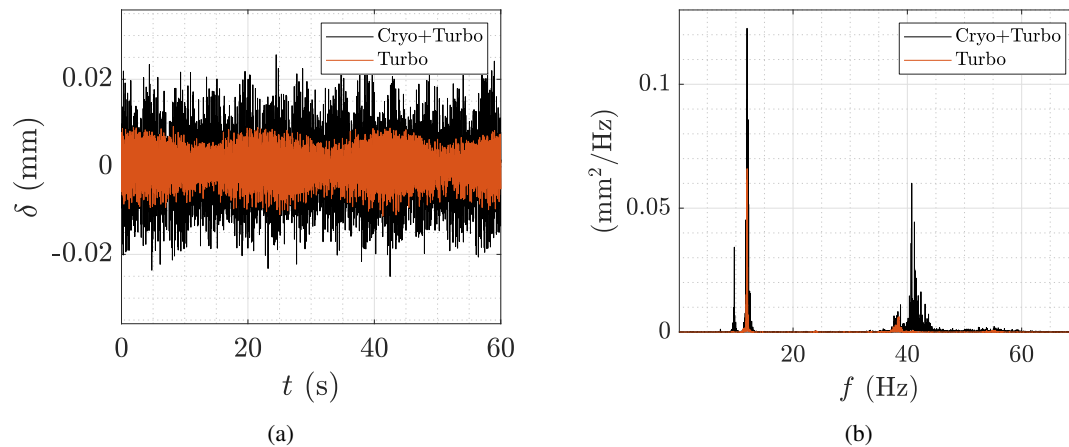


FIG. 8: Oscillations induced by pumps on the (a) thrust stand and (b) power spectral density of these oscillations.

A. Vibrational Noise Analysis

The thrust stand is subject to a variety of external sources for vibration. These can impact the error and sensitivity of the measurements. In our case, the dominant contributor is the vibration of the facility turbo and cryogenic pumps, which operate at 500 Hz and 2 Hz, respectively. To quantify the impact of these pumps on the thrust stand operation, we measured the displacement on the thrust stand without the thruster operating. This provided a baseline on the mechanical noise level. We note here that for the tests presented in this article, we used both the turbo and cryogenic pumps to minimize base pressure during testing. However, in some use cases, we only operate the turbopump. To be comprehensive in our analysis of this noise source, we thus also measured the displacement with only the turbopump running.

Figure 8a shows the displacement sensor output during these tests measured at a sampling rate of 200 samples/s. Figure 8 shows the power spectral density for these data. This power spectral density plots indicate that the ambient displacement data measured with only the turbopump operating had a dominant frequency of 11.9 Hz while the cryogenic pump added noise at 9.7 and 40.7 Hz. The former show RMS displacements on the order of 5 and 15 μm for the turbo and cryogenic pump cases, respectively. Based on the first order dynamical analysis in Appendix C, the thrust stand pendulum should damp vibrations under $f \approx 0.3$ Hz. Thus the oscillations seen in the ambient data are likely higher order resonances within the structure.

Absent averaging, this noise level would translate approximately to a measurement uncertainty of 0.5 mN. However, as we discuss in the following section, the cyclical nature of these oscillations allows them to be averaged out using a moving average filter. We typically did this averaging over a period of five seconds.

B. Thermal Drift Characterization

In this section, we characterize the thrust stand's response to thermal loading caused by changes in thruster temperature. Separating thermal drift from thrust force is critically important for achieving accurate measurements. While some level of thermal drift is acceptable, it is important that this drift remains linear over the time period required for measuring thrust. This allows for linear corrections to be applied to the raw data.

We test the thrust stand's thermal stability by attaching a high power RF termination (a "dummy load") in place of the thruster. We apply 30 watts of RF power to the dummy load (at vacuum) for fifteen minutes and record temperature and displacement, as shown in Fig. 9a. In Fig. 9b, we focus on the 90 seconds before and after power is turned off, as this most closely represents a thrust measurement. The results show the thermal drift, which is manifested as a systematic decrease in the displacement measurement. We see, however, that the displacement is approximately linear over the timescales relevant to thrust measurements (~ 40 seconds). This region of linearity is emphasized in Fig. 9b with vertical black lines. The blue dotted line shows the linear trend, -4.7×10^{-3} mm/minute, which equates to -0.08 mN/minute for this measurement. This is in range with comparable thrust stands. It should be noted that this number is a maximum as the drift rate significantly decreases as the thruster reaches thermal steady state. These plots suggest that we can correct for thermal drift by fitting a line to the displacement and subtracting the resulting slope from the data.

As an aside, we briefly comment here on the underlying causes of this thermal drift. The predominant source of thermal drift in traditional thrust stands— the expansion of the RF cable spanning the fixed and swinging parts of the thrust stand— was

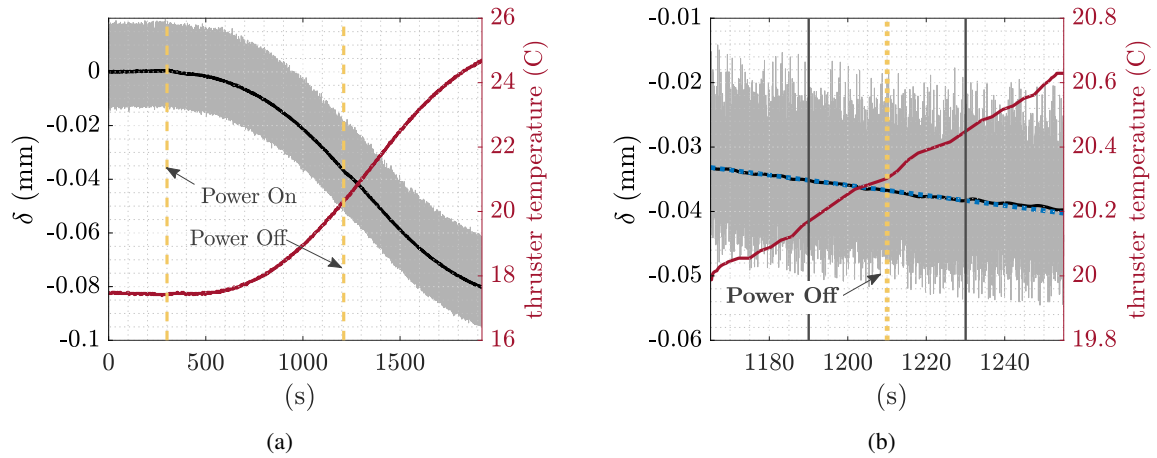


FIG. 9: Displacement and temperature data during dummy load test (a). The vertical yellow lines show the times when power to the dummy load (30 W) is turned on and off. The zoomed in view (b) shows the displacement trend (blue line, -4.7×10^{-3} mm/minute) and time required for taking a thrust measurement (black vertical lines).

C. Calibration

In this section, we provide the results of thrust stand calibrations with the vertical counterweight positioned at two locations: its upper limit (1 mm from the top) and an intermediate position 80 mm from the top to demonstrate its variable sensitivity. In these tests, we have set the calibration rig to use two independent calibration masses for a total of three calibration test points. The total mass and equivalent thrust force for each test point are shown in Table II.

TABLE II: Calibration points

Test Point	Weights Used	Total Mass (g)	Equivalent Thrust Force (mN)
1	1	0.0495	0.1618
2	2	0.1798	0.5878
3	1+2	0.2293	0.7496

The procedure for calibration is as follows: The thrust stand records ambient data to measure any linear drifts that may be occurring. Each weight is then placed on the calibration bar in ascending order. The weights are then removed in the reverse order yielding the plot shown in grey in Fig. 10a and 10b. Here, we have taken data at 200 samples/s and held each calibration point for 15 seconds. In post-processing, we applied a Gaussian moving average filter with a 5 second (1000 sample) window and a 1 second (200 sample) standard deviation to smooth the data and eliminate the noise from pump-induced vibrations. The filtered results are shown in black in Fig. 10a and orange in Fig. 10b. We used a least squares regression to fit a line to the first 12 seconds of data (prior to dropping any weights) to determine the thrust stand's thermal drift. Using this linear fit, we detrended the data by subtracting the slope of the line from the displacement using $t = 12$ s as an intercept. We take the individual calibration points using the smoothed data recorded 12 seconds after dropping or picking up each weight (shown in blue in Fig. 10a). We fit the calibration data using a least squares linear regression, shown in Fig. 10c. Typically, we perform a calibration before each thrust test point to ensure accuracy.

The data show that the thrust stand has a sensitivity of -0.0580 mm/mN (-17.24 mN/mm) with the counterweight at the top position and -0.0247 mm/mN (-40.49 mN/mm) with the counterweight 80 mm from the top. This is comparable to other thrust stands in this class [24, 26]. Close inspection of Fig. 10a and Fig. 10b shows that there is less overshoot and thus lower settling times for the thrust stand configured with the counterweight at the bottom. However, positioning the counterweight at the top

provided over twice the resolution. Because the settling time was on the order of a few seconds, most of our testing used the top counterweight position.

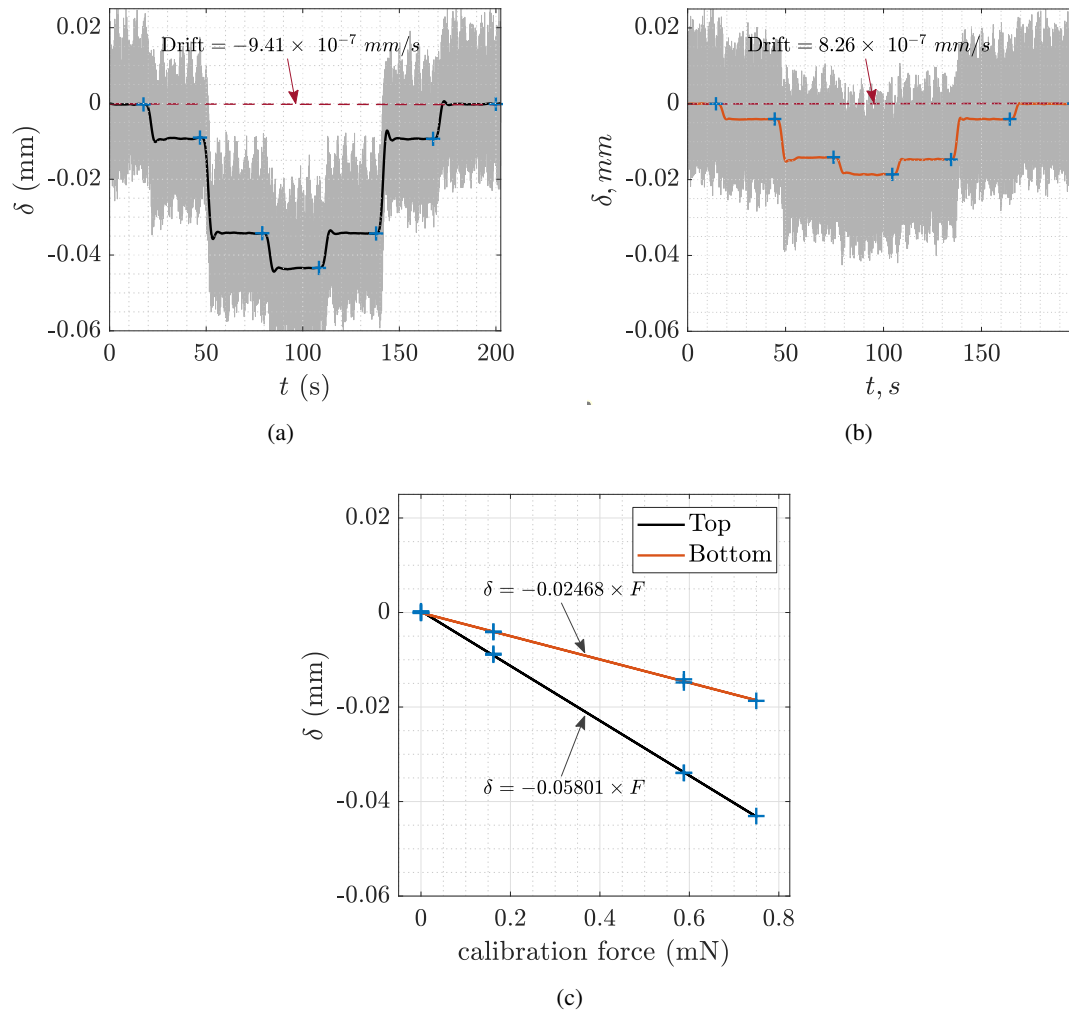


FIG. 10: Calibration data showing the raw and smoothed displacements for the counterweight in the top (a) and 80 mm from the top (b) configurations. Linear fit of the calibration data for each counterweight position (c).

D. Electrostatic Testing

Many thruster configurations, including those used in this investigation, require testing with an electrically floating thruster body. Previous tests on ECR thrusters have shown that thruster floating potential can reach as high as 200 V [29]. Here, we test the effects of electrostatic charging of the thruster body by attaching a conductive lead to the thruster and sweeping a voltage from 0-200 V while concurrently measuring displacement. We show the results of this experiment in Fig. 11. The data indicate that displacement is not affected by thruster floating potential, within the limits of our measurements, thus eliminating this effect as a source of error.

E. Uncertainty Analysis

In this section, we provide an overview of potential sources of error for the thrust measurements and then combine these to assess the relative uncertainty in our results. To this end, the predominant errors stem from the physical lengths of the pendulum (l_T) and calibration arm (l_{cal}), the slope of the calibration line (k_{cal}), and uncertainty in the measured displacement (δ). These

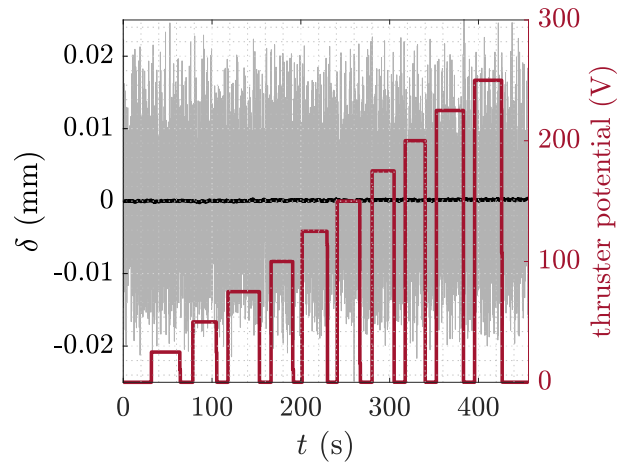


FIG. 11: Measured displacement as the electrostatic potential is varied. The black line denotes the filtered average.

uncertainties compound to yield [4] a relative uncertainty in the thrust measurement:

$$\frac{\sigma_T}{T} = \left[\left(\frac{\sigma_\delta}{\delta} \right)^2 + \left(\frac{\sigma_{k_{cal}}}{k_{cal}} \right)^2 + \left(\frac{\sigma_{l_t}}{l_t} \right)^2 + \left(\frac{\sigma_{l_{cal}}}{l_{cal}} \right)^2 \right]^{1/2}, \quad (5)$$

where σ denotes the uncertainty in the indicated parameter.

The geometric uncertainty of l_T and l_{cal} is based on manufacturing tolerances. For our thrust stand design we estimate these values to be $\sigma_{l_T} \approx \sigma_{l_{cal}} \approx 1$ mm. To determine the uncertainty with the displacement sensor, σ_δ , we recall from Fig. 8 that the dominant source of variance in this signal is the periodic vibration induced by the pumps. While this can be eliminated by averaging over longer periods, extending the averaging period to too long of a period will introduce systematic error from the thermal drift. In light of these constraints, our thermal study showed (Figure 9b) the maximum amount of allowable time for averaging was approximately 20 seconds. For our work, we have chosen an intermediate averaging period of five seconds. With this value in mind, we calculate the error in δ by first applying a five-second moving average to our ambient data. We then take the standard deviation of this moving average over a 60 second period to determine σ_δ . Using the data in Fig. 8, we find a standard deviation of $\sigma_\delta = 8 \times 10^{-5}$ mm. It should be noted that this process differs from that listed in Ref.[4], which we believe underestimates the displacement error for our system.

To estimate the uncertainty in the calibration slope, $\sigma_{k_{cal}}$, we used the procedure outlined in Ref. [4]. This is based on taking the standard deviation of a series of calibration measurements:

$$\sigma_{k_{cal}} \approx s_{K_{cal}} = \frac{s_\delta}{\sqrt{\sum_{i=1}^n (F_i - \bar{F})^2}}, \quad (6)$$

where $s_{K_{cal}}$ is the standard deviation of the calibration slope, s_δ is the standard deviation of the time-averaged displacement (calculated from σ_δ), F_i is a sample calibration force, and \bar{F} is the average of the applied calibration forces. For our calculation of $\sigma_{k_{cal}}$, we take 21 sample calibration points (shown in Fig 12), which yields $\sigma_{k_{cal}} = 5.8 \times 10^{-5}$ mm/mN.

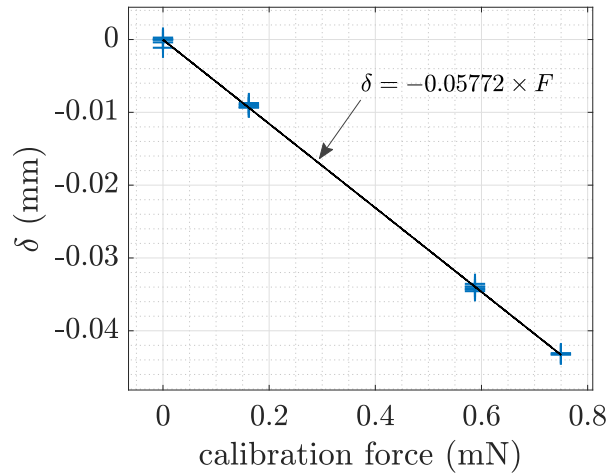


FIG. 12: Calibration points used for determining σ_{kcal} .

With these estimates for uncertainty and following in Eq. 5, we show in Fig. 13 the 95% confidence interval ($2\sigma_T/T$) for each measured thrust. We see from this result that the measurement uncertainty error is dominated by the displacement error, σ_T/T , for thrust values above 0.1 mN.

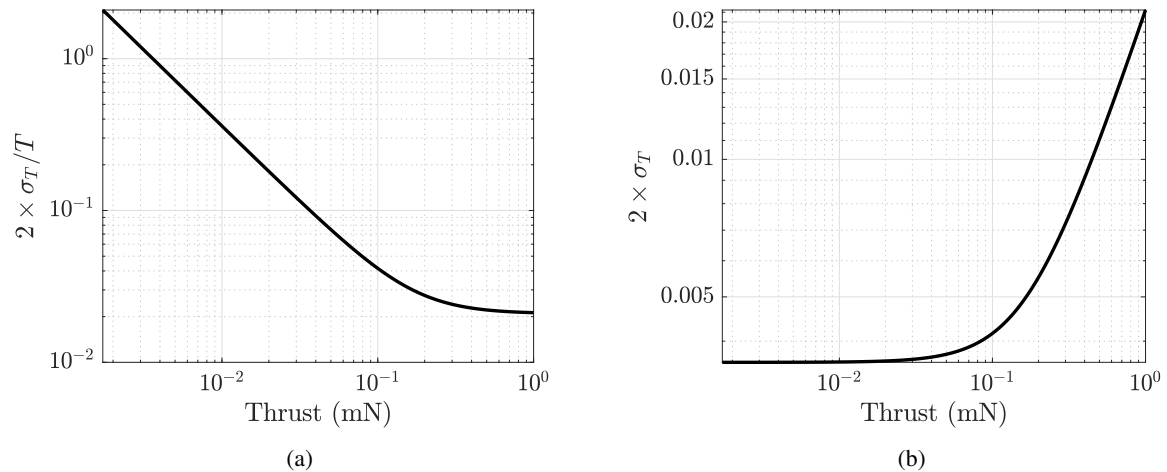


FIG. 13: 95% confidence interval for (a) relative thrust measurements ($2\sigma_T/T$) and absolute thrust ($2\sigma_T$) as a function of measured thrust.

F. Thruster Testing

In this section we present the results of our ECR thruster tests. We generate thrust data by measuring the difference in thruster stand displacement between on and off states. The power delivered to the thruster, P_{rf} , is determined by subtracting the reflected power from the forward power, as measured at the directional coupler. The thrust measurement procedure is as follows. Once the thruster reaches a quasi-steady state, as determined by observing forward and reflected powers, we gather 30 seconds of thruster-on data. We then turn the thruster off and measure the change in displacement. In the case of cold-gas thrust, we shut a valve flowing gas to the thruster. The data are post-processed using a similar technique to the calibration procedure described in Sec. III B. We use a five second Gaussian moving average filter to smooth the data. We then fit a line to the first 12 seconds of displacement data to determine the drift and subtract this slope from the data, using the displacement at $t = 12$ s seconds as an intercept. We use the filtered and detrended points taken 12 seconds before and 12 seconds after shut-off for calculating thrust.

Figure 14 shows a typical cold gas thrust measurement using 5 sccm xenon. Translating the displacement data to force measurements via Eq. 1 yields a total thrust of 0.065 ± 0.0033 mN. We show a typical thrust measurement for a 24 watt (measured as delivered power), 1 sccm xenon operating condition in Fig. 15a. The detrended displacement is shown in Fig. 15b.

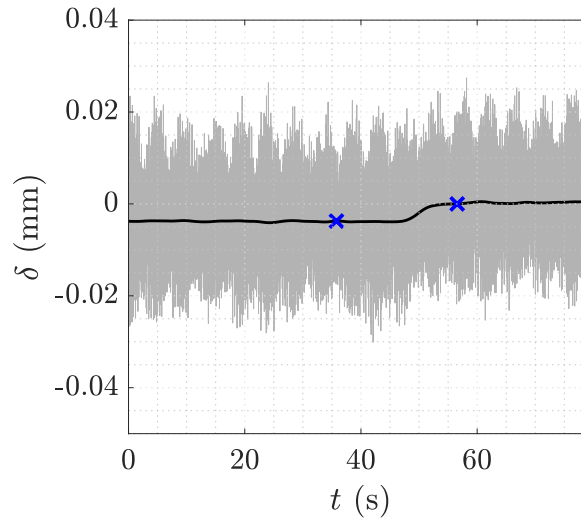


FIG. 14: Cold gas thrust measurement for 5 sccm xenon. Gas is shut off at 40 seconds. The gray line shows the unfiltered displacement data. The black line denotes the output of a 5 second Gaussian moving average filter. The blue x's denote the data points used for determining thrust.

We note here a few subtleties of the thrust measurements. First, the position of the displacement sensor (Fig. 2C), yields negative values of δ for positive thrust. Second, in this measurement, the blue X's denote the data points used in determining thrust. These correspond to the five second averaged data 12 seconds before and after power shutoff. Third, the thrust trace demonstrates some of the dynamic responses inherent to the thrust stand design. We can see a small overshoot in the averaged displacement, which is a consequence of the thrust stand being an under-damped system. Fourth, we can also see in the detrended data that the data begins to slope downward after ~ 60 seconds. This is caused by the thermal drift becoming increasingly non-linear after ~ 15 seconds, as was shown in Sec. V B.

The data for the 24 watt, 1 sccm measurement provides a measured thrust of 0.408 ± 0.009 mN. From this, we can calculate specific impulse (I_{sp}) and efficiency (η) metrics using $I_{sp} = F_T / (\dot{m}g)$ and $\eta = F_T^2 / (2\dot{m}P_{rf})$ where \dot{m} is the propellant mass flow rate and P_{rf} is the absorbed power as measured at the directional coupler. Here, we find a specific impulse of $I_{sp} = 408 \pm 10$ s and an efficiency $\eta = 3.85 \pm 0.17\%$.

To illustrate the range of the thrust stand to resolve thrust levels, we show in Fig. 16 parametrically swept measurements of the thrust, specific impulse, and efficiency for 1 sccm and 10 sccm flow rates. It should be noted that the error bars shown incorporate only the uncertainty in the thrust measurement and do not include the error stemming from uncertainty in flow rate and delivered microwave power.

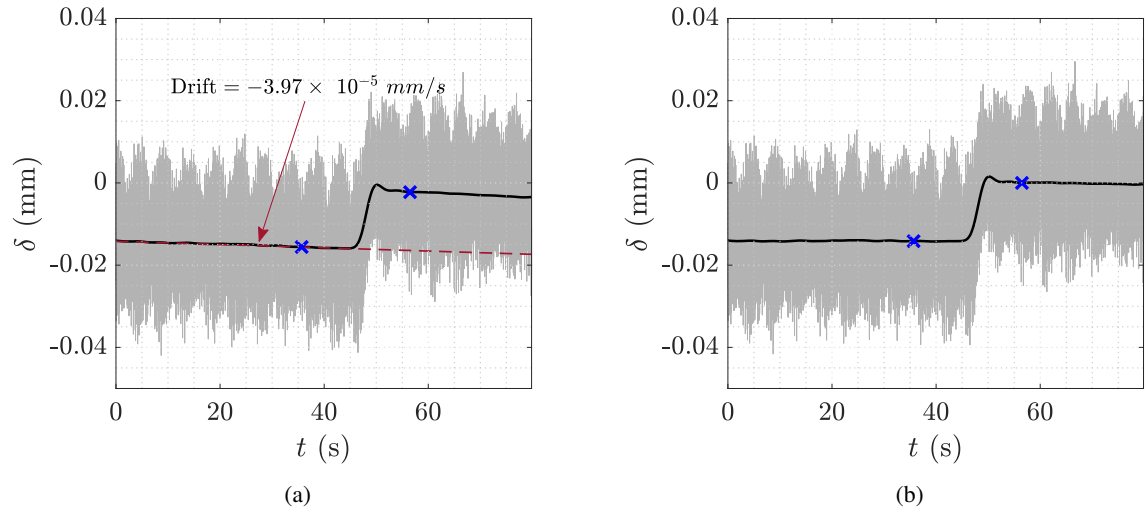


FIG. 15: Thrust data for 24 W delivered power, 1 sccm Xe operating point, (a) shows the raw and smoothed displacement and (b) shows the detrended data. The blue x's denote the data points used for determining thrust.

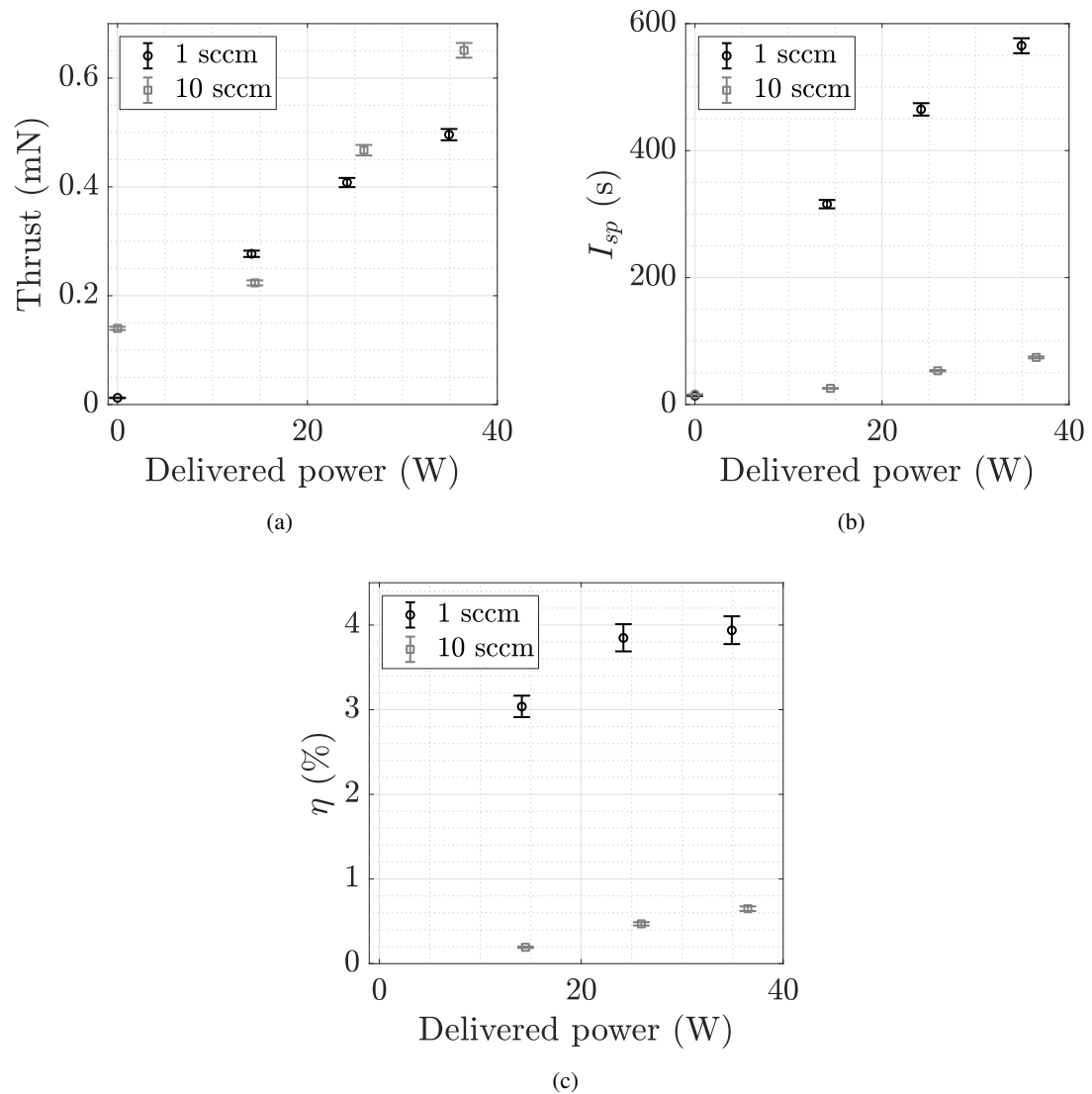


FIG. 16: ECR thrust performance at 1 and 10 sccm xenon flow rates showing thrust (a), specific impulse (b), and efficiency (c) vs. power. The zero power data points correspond to cold gas measurements.

The data show that low flow rates yield much higher thruster performance. This effect is commonly seen in ECR and other magnetic nozzle thrusters [30]. It stems largely from the lower specific power inherent to high flow rates, but can also be exacerbated by facility effects caused by high background pressures associated with the increased flow rates [31].

We illustrate the broad-band capabilities of the wireless power coupler in Fig. 17. Here, we have measured thrust as a function of frequency for a set absorbed power (30 W) and flow rate (2 sccm Xe). Before taking these measurements, we first determine the attenuation of the thrust stand cabling and wireless coupler before conducting the experiment using a power sensor in place of the thruster. The power reflected by the thruster is shown on the right hand side of the plot. Comparing these reflected power values to the coupler's reflection coefficient, S_{11} , in Fig. 5a, we see that the system's reflection coefficient is dominated by plasma effects, as it does not follow the same trends as the wireless power coupler. This result indicates that wireless power coupler does not adversely effect test performance. However, a more complete determination of the reflected power must take into account finite directivity effects inherent to directional coupler measurements [27, 32]. This result thus highlights the broadband capabilities of the thrust stand, which are necessary for the parametric investigation of the frequency dependence of the performance of this thruster.

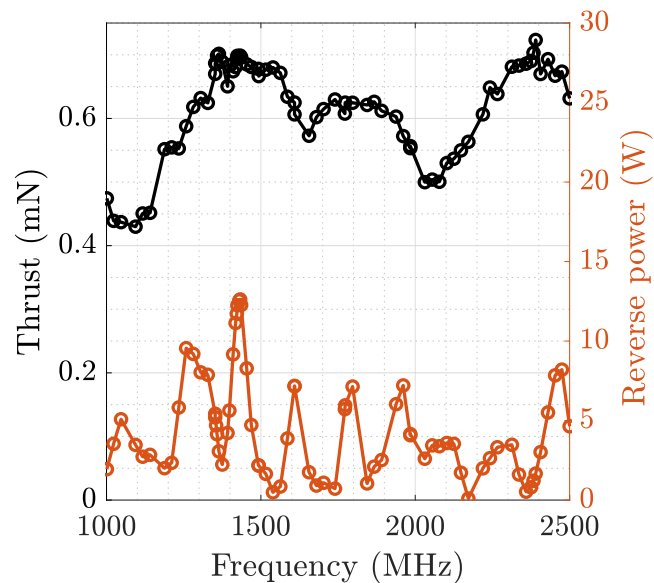


FIG. 17: Thrust measurements for a range of frequencies from 1000 to 2500 MHz, with the thruster set to 30 W absorbed power, 2 sccm xenon flow rate operating condition. The reverse power is plotted on the right axis.

VI. DISCUSSION

Using Fig. 16, we can examine some of the general trends seen in our thrust measurements. The data show that the 10 sccm cold gas operation produces $\sim 10\times$ the thrust of the 1 sccm cold gas point. This demonstrates that specific impulse is nearly constant for cold gas operation, as would be expected for this design. We can further observe that, at low powers, the cold gas thrust accounts for a large portion of the total thrust produced during the thruster's high flow-rate operation. This points to one of the most commonly observed properties of these thrusters: thrust efficiency scales with specific power [5]. This effect is prominent enough that high flow rates can even impede thrust generation in these devices, as seen in the 15 W data points in Fig. 16(a).

The thrust measurements also provide some context for the thrust stand's sensitivity and uncertainty characteristics. Figure 16(a) demonstrates the thrust stand's ability to detect thrust less than the force produced by 1 sccm of cold gas—typically a lower force bound for this class of thrusters. By repeatedly running these cold gas thrust tests, we were able to consistently resolve $\sim 10\ \mu\text{N}$ forces, providing us with an upper bound on force resolution. The uncertainty analysis suggests that the measurement error is nearly constant for forces above $\sim 0.2\ \text{mN}$. This stems from the fact that the error caused by dimensional tolerances and uncertainty in the slope of the calibration line cause errors that scale directly with thrust, while the uncertainty caused by random vibrational fluctuations is independent of measured thrust. Therefore as thrust increases, the relative impact of the random vibrational error diminishes to an almost negligible amount. While we were able to accommodate some level of thermal drift by post processing the data, future design could ameliorate these issues by incorporating more thermal mass around the pivots, or employing active heating or cooling.

The uncertainty and resolution measured in our tests are comparable to other thrust stands intended for this class of EP thruster [9, 14, 24, 33]. It should be noted that while higher resolution design exist, they are generally intended for lower thrust technologies i.e. electrospray and cold gas thrusters [34–36].

Finally, the test results provided in Fig. 17 show the wireless coupler and thrust stand's ability to perform broadband microwave testing. Tests such as these allow for waveform optimization experiments in which the input microwave power characteristics are swept over several points throughout a test. Given the short (~ 1 minute) thrust measurement time, the thrust stand enables hundreds of points to be gathered in the span of a few hours. However, it should be noted that a more comprehensive efficiency analysis would require consideration of the directional coupler's directivity to determine the uncertainty bounds on the absorbed microwave power [27, 32].

VII. CONCLUSION

We have presented the design and performance of a variable-sensitivity hanging pendulum thrust stand for measuring sub-millinewton forces. We demonstrated the ability to change the thrust stand's sensitivity from 40.49 mN/mm to 17.24 mN/mm by moving its vertical counterweight. We additionally described the design and performance of a novel high bandwidth wireless power coupler for mitigating the effects of RF cable expansion during microwave-powered thruster testing. The thrust stand was tested using a low-power ECR thruster, demonstrating the ability to resolve $\sim 0.065 - 0.4\mu\text{N}$ forces, with error under 3% for thrust levels above 0.1 mN. We tested the effects of environmental vibration, thermal drift, and electrostatic charge on the performance of the thrust stand. The thrust stand exhibited non-negligible thermal drift on the timescales relevant to thrust measurements; however, this drift remained linear over the ~ 20 seconds needed to measure thrust. Electrostatic charging was shown to have no effect on thrust readings. Our error analysis showed a minimum viable thrust measurement on the order $\sim 10\mu\text{N}$, less than the thrust produced by ~ 1 sccm xe cold gas thrust. The movable counterweight gives the thrust stand the ability to adjust between low-settling time and high accuracy settings. While this feature was not utilized extensively in our testing (largely due to the longer thruster settling times), it could provide a valuable asset for future optimization experiments requiring faster measurement times. Overall, this design provides an architecture capable of measuring the thrust range expected by most low-power magnetic nozzle thrusters, while the sensitivity and inherent uncertainty provide enough resolution for discriminating between small design changes.

ACKNOWLEDGMENTS

This work was supported by NASA Space Technology Research Fellowship grant 80NSSC17K0157. The authors would like to thank Eric Viges for his help in setting up the vacuum facilities and Terry Larrow for his help in constructing the thrust stand.

Appendix A: Thrust Stand Static Model

Using Fig. 1 as a reference, we derive a static sum of moments as follows:

$$0 = -F_T l_T - m_{CW} g (l_{CW} \sin(\theta) - d_{CW} \cos(\theta)) - m_{cal} g l_{cal} \cos(\theta) - m_{arm} g l_{arm} \cos(\theta) + m_T g (l_{COM} \sin(\theta) - d_{COM} \cos(\theta)) + k\theta, \quad (\text{A1})$$

where F_T is the thrust force, l_T is the length from the pivot to the center of thrust, m_{cal} is the added calibration mass, and l_{cal} is the length from the pivot to the location where the calibration masses are applied. The lengths d_{CW} , l_{CW} , d_{COM} , and l_{COM} are the horizontal and vertical distances from the center of masses of the counterweight (CW) and thruster (COM) to the pivot point. We use the convention shown in Fig. 1 to denote the direction of these measurements. The length l_{arm} is the horizontal length of the center of mass of the calibration arm. The dimensions and masses, m_{CW} , m_T , and m_{arm} include support structure masses.

Employing the small angle approximation simplifies Eq. A1 to

$$0 = -F_T l_T - m_{CW} g (l_{CW} \theta - d_{CW}) - m_{cal} g l_{cal} - m_{arm} g l_{arm} + m_T g (l_{COM} \theta - d_{COM}) + k\theta. \quad (\text{A2})$$

Solving for θ gives:

$$\theta = \frac{-F_T l_T + m_{CW} g d_{CW} - m_{cal} g l_{cal} - m_{arm} g l_{arm} - m_T g d_{COM}}{m_{CW} g l_{CW} - m_T g l_{COM} - k}. \quad (\text{A3})$$

We can now solve for the measurable quantity, δ_{disp} , by making the substitution $\delta_{disp} = \delta_0 - l_{sens} \sin(\theta)$, where δ_0 is the distance to the sensor when $\theta = 0$. Again employing the small angle approximation, we find

$$\theta = \frac{\delta_0 - \delta_{disp}}{l_{sens}}. \quad (\text{A4})$$

Substituting this expression into Eq. A3 and solving for δ_{disp} gives:

$$\delta_{disp} = -l_{sens} \left[\frac{-F_T l_T + m_{CW} g d_{CW} - m_{cal} g l_{cal} - m_{arm} g l_{arm} - m_T g d_{COM}}{m_{CW} g l_{CW} - m_T g l_{COM} - k} + \delta_0 \right]. \quad (\text{A5})$$

From Eq. A5, we can derive the change in displacement, $\Delta\delta_{disp}$, caused by changes in thrust (F_T) and changes in calibration mass (m_{cal}):

$$\Delta\delta_{disp} = l_{sens} \left[\frac{(F_T - F_{T,0}) l_T + (m_{cal} - m_{cal,0}) g l_{cal}}{m_{CW} g l_{CW} - m_T g l_{COM} - k} \right], \quad (\text{A6})$$

where $F_{T,0}$ and $m_{cal,0}$ are initial thrust and calibration forces, typically 0 for our purposes. We can thus relate the displacement to changes in thrust by setting $m_{cal} = m_{cal,0} = 0$. Simplifying the resulting expression yields

$$\Delta\delta_{disp} = A_T F_T + b_{T,0}, \quad (A7)$$

where the slope of the line, A_T , is given by

$$A_T = l_{sens} \frac{l_T}{m_{CW} g l_{CW} - m_{COM} g l_{COM} - k}. \quad (A8)$$

Appendix B: Relation Between Calibration and Thrust Forces

Using Eq. A6 we solve for the displacement caused by changes in calibration mass by setting $F_T = T_{T,0} = 0$. Simplifying the resulting expression yields

$$\Delta\delta_{cal} = A_{cal} F_{cal} + b_{cal,0}, \quad (B1)$$

where the calibration force $F_{cal} = g m_{cal}$. The slope of the calibration line, A_{cal} , is given by

$$A_{cal} = l_{sens} \frac{l_{cal}}{m_{CW} g l_{CW} - m_{COM} g l_{COM} - k}. \quad (B2)$$

Using Eqs. B2 and A8 we can relate the displacement caused by thrust force to that from calibration force as

$$\frac{A_T}{A_{cal}} = \frac{l_T}{l_{cal}}. \quad (B3)$$

Thus applying a force F at the calibration arm is equivalent to applying a force $F \frac{l_{cal}}{l_T}$ at the thruster.

Appendix C: Thrust Stand Dynamic Model

From the thrust stand geometry, we can estimate the thrust stand's eigenfrequency using a simple harmonic oscillator model:

$$f_0 = \frac{1}{2\pi} \sqrt{\frac{g(m_{CW} l_{CW} + m_T l_T) - K}{m_T l_T^2 + m_{CW} l_{CW}^2}}. \quad (C1)$$

Using the values shown in Table I, we find that the natural oscillating frequency to be $f_0 \approx 0.3$ Hz.

We can perform a more comprehensive dynamical analysis following the approach given in Ref. [20]. Here, we calculate the thrust stand's response to non-constant thrust forces using

$$H(i\omega) = \frac{S_{sens}}{\left(\frac{i\omega}{\omega_0}\right)^2 + 2\zeta \frac{i\omega}{\omega_0} + 1}, \quad (C2)$$

where S_{sens} is the fiber-optic sensor's sensitivity in V/mm, ω_0 is the resonant frequency in rad/s, and ζ is the damping ratio, which we assume to be 0.5. We show the calculated normalized transfer function in Fig. 18, where $H(i\omega)$ has been normalized by its DC value.

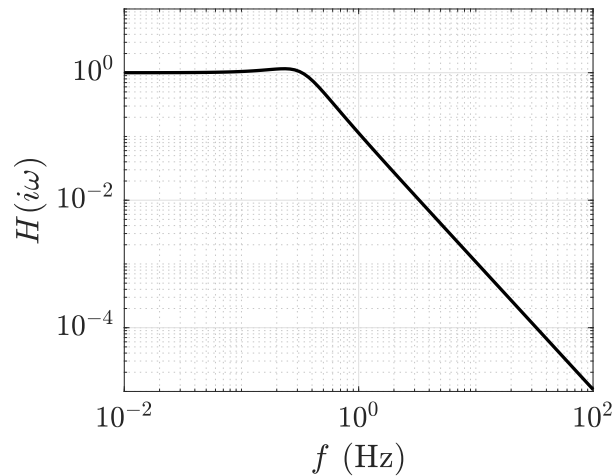


FIG. 18: Normalized thrust transfer function showing relative displacement as a function of thrust excitation frequency.

DATA AVAILABILITY STATEMENT

The data that support the findings of this study are available from the corresponding author upon reasonable request.

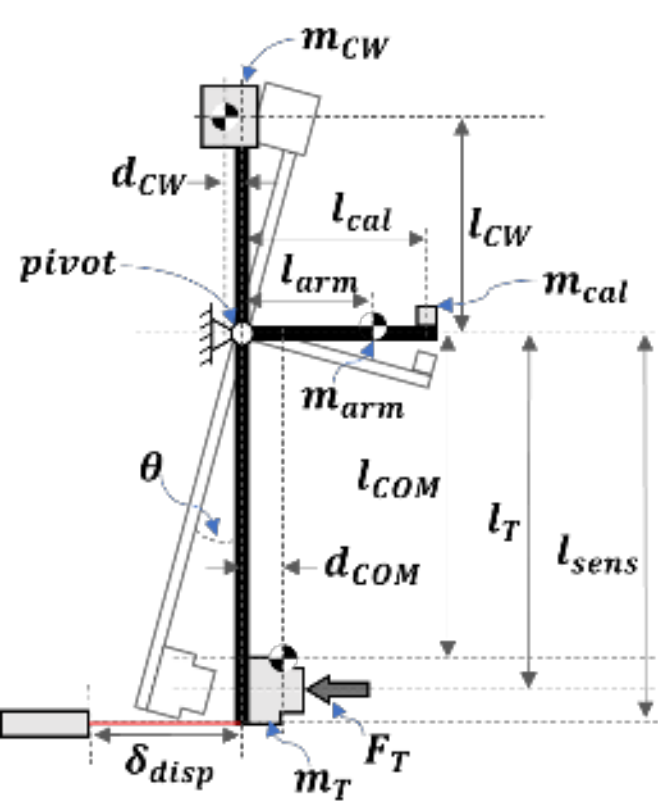
REFERENCES

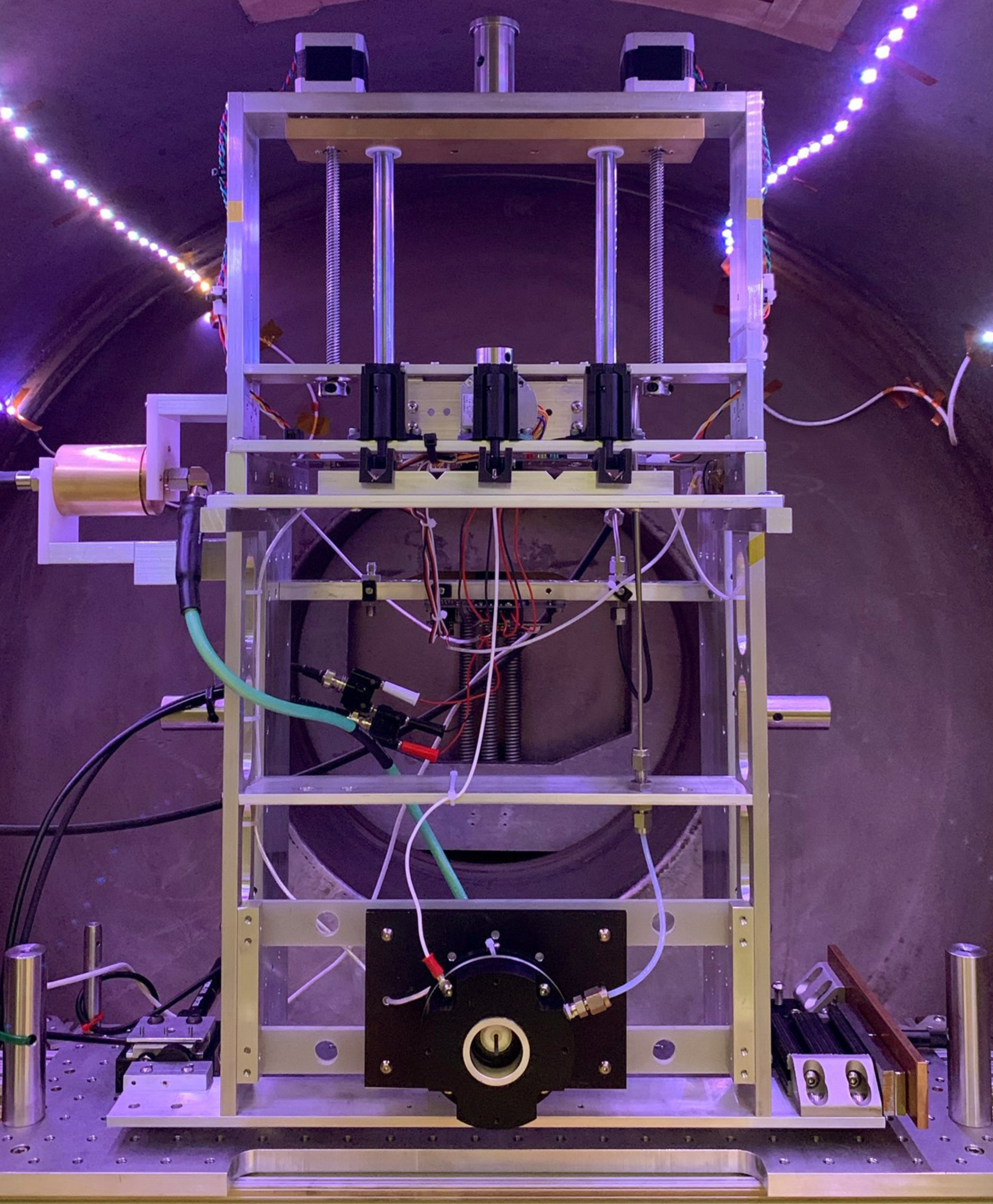
- [1] K. Holste, P. Dietz, S. Scharmann, K. Keil, T. Henning, D. Zschätzsch, M. Reitemeyer, B. Nauschütt, F. Kiefer, F. Kunze, J. Zorn, C. Heiliger, N. Joshi, U. Probst, R. Thüringer, C. Volkmar, D. Packan, S. Peterschmitt, K. T. Brinkmann, H.-G. Zaunick, M. H. Thoma, M. Kretschmer, H. J. Leiter, S. Schippers, K. Hannemann, and P. J. Klar. Ion thrusters for electric propulsion: Scientific issues developing a niche technology into a game changer. *Review of Scientific Instruments*, 91(6):061101, June 2020.
- [2] Dan Lev, Roger M. Myers, Kristina M. Lemmer, Jonathan Kolbeck, Hiroyuki Koizumi, and Kurt Polzin. The technological and commercial expansion of electric propulsion. *Acta Astronautica*, 159:213–227, June 2019.
- [3] Igor Levchenko, Kateryna Bazaka, Yongjie Ding, Yevgeny Raitses, Stéphane Mazouffre, Torsten Henning, Peter J. Klar, Shunjiro Shinohara, Jochen Schein, Laurent Garrigues, Minkwan Kim, Dan Lev, Francesco Taccogna, Rod W. Boswell, Christine Charles, Hiroyuki Koizumi, Yan Shen, Carsten Scharlemann, Michael Keidar, and Shuyan Xu. Space micropropulsion systems for Cubesats and small satellites: From proximate targets to furthestmost frontiers. *Applied Physics Reviews*, 5(1):011104, March 2018.
- [4] James E. Polk, Anthony Pancotti, Thomas Haag, Scott King, Mitchell Walker, Joseph Blakely, and John Ziemer. Recommended Practice for Thrust Measurement in Electric Propulsion Testing. *Journal of Propulsion and Power*, 33(3):539–555, May 2017.
- [5] F. Cannat, T. Lafleur, J. Jarrige, P. Chabert, P.-Q. Elias, and D. Packan. Optimization of a coaxial electron cyclotron resonance plasma thruster with an analytical model. *Physics of Plasmas*, 22(5):053503, May 2015.
- [6] Benjamin W. Longmier, Bryan M. Reid, Alec D. Gallimore, Franklin R. Chang-Diaz, Jared P. Squire, Tim W. Glover, Greg Chavers, and Edgar A. Bering. Validating a Plasma Momentum Flux Sensor to an Inverted Pendulum Thrust Stand. *Journal of Propulsion and Power*, 25(3):746–752, May 2009.
- [7] Daniel G. Courtney, Simon Dandavino, and Herbert Shea. Comparing Direct and Indirect Thrust Measurements from Passively Fed Ionic Electro spray Thrusters. *Journal of Propulsion and Power*, 32(2):392–407, March 2016.
- [8] Kazunori Takahashi, Takeharu Sugawara, and Akira Ando. Spatially- and vector-resolved momentum flux lost to a wall in a magnetic nozzle rf plasma thruster. *Scientific Reports*, 10(1):1061, January 2020. Number: 1 Publisher: Nature Publishing Group.
- [9] Théo Vialis, Julien Jarrige, Ane Aanesland, and Denis Packan. Direct Thrust Measurement of an Electron Cyclotron Resonance Plasma Thruster. *Journal of Propulsion and Power*, 34(5):1323–1333, 2018.
- [10] Emmanuelle Rosati Azevedo, Kyaw Swar, Daniel Staab, Emily Longhi, Alberto Garbayo, Burak Karadag, James Stubbing, Rachel Moloney, Andrea Fabris, Thomas Toux, Olli Tarvainen, and Daniel Faircloth. XJET: Design Upgrade and Preliminary Characterization for an Electrodeless ECR Thruster. Estoril, Portugal, March 2021.
- [11] Jeffrey R. Hopkins, Michael M. Micci, Sven G. Bilén, and Silvio G. Chianese. Direct Thrust Measurements of an 8-GHz Microwave Electrothermal Thruster. *IEEE Transactions on Plasma Science*, 46(6):2009–2015, June 2018. Conference Name: IEEE Transactions on Plasma Science.

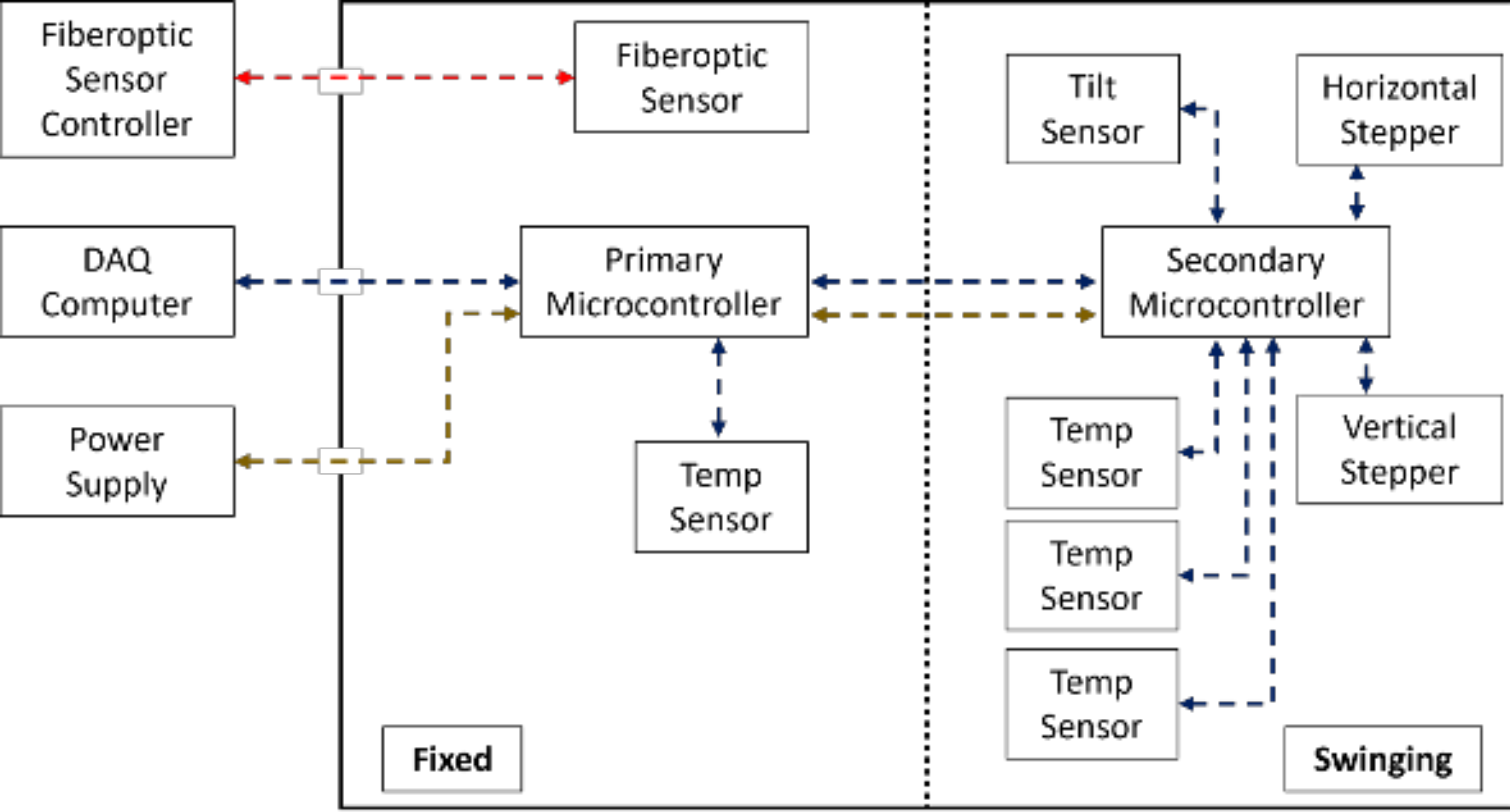
This is the author's peer reviewed, accepted manuscript. However, the online version of record will be different from this version once it has been copyedited and typeset.

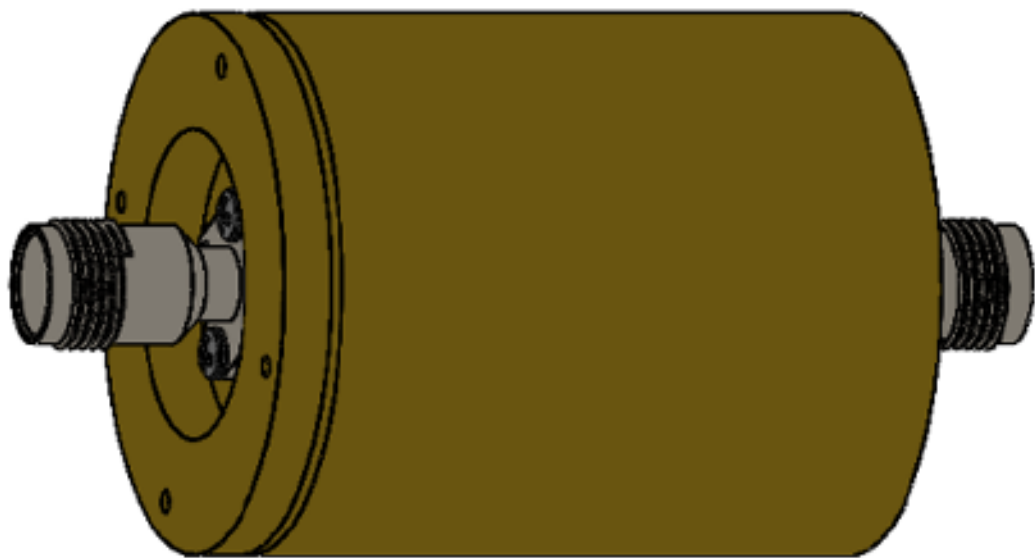
PLEASE CITE THIS ARTICLE AS DOI:10.1063/1.5008831

- [12] Y. Tani, R. Tsukizaki, D. Koda, K. Nishiyama, and H. Kuninaka. Performance improvement of the μ 10 microwave discharge ion thruster by expansion of the plasma production volume. *Acta Astronautica*, 157:425–434, April 2019.
- [13] S Peterschmitt and D Packan. Comparison of Waveguide Coupled and Coaxial Coupled ECRA Magnetic Nozzle Thruster using a Thrust Balance. In *36th International Electric Propulsion Conference*, September 2019.
- [14] K Swar, D Staab, A Garbayo, L Shadbolt, S Masillo, A Lucca Fabris, B Karadag, and R Moloney. Design and testing of a μ N - mN torsional thrust balance with wireless microwave power transmission. Vienna, Austria, September 2019.
- [15] Michael McDonald, Michael Nurnberger, and Logan Williams. Preparations for Thrust Measurement and Error Discussion of the IMPULSE Resonant Microwave Cavity. Atlanta, GA, October 2017.
- [16] Benjamin Wachs and Benjamin Jorns. Optimization of an ECR Thruster using Two Frequency and Pulsed Waveforms. In *AIAA Propulsion and Energy 2021 Forum, VIRTUAL EVENT*, August 2021. American Institute of Aeronautics and Astronautics.
- [17] J. Jarrige, P. Thobois, C. Blanchard, P.-Q. Elias, D. Packan, L. Fallerini, and G. Noci. Thrust Measurements of the Gaia Mission Flight-Model Cold Gas Thrusters. *Journal of Propulsion and Power*, 30(4):934–943, July 2014.
- [18] Kevin Diamant, James Pollard, Mark Crofton, Michael Patterson, and George Soulas. Thrust Stand Characterization of the NASA NEXT Thruster. In *46th AIAA/ASME/SAE/ASEE Joint Propulsion Conference & Exhibit*, Nashville, TN, July 2010. American Institute of Aeronautics and Astronautics.
- [19] Franz Georg Hey. *Micro Newton Thruster Development*. Springer Fachmedien Wiesbaden, Wiesbaden, 2018.
- [20] Denis Packan, Jean Bonnet, and Simone Rocca. Thrust Measurements with the ONERA Micronewton Balance. September 2007.
- [21] S. J. Pottinger, D. Lamprou, A. K. Knoll, and V. J. Lappas. Impact of plasma noise on a direct thrust measurement system. *Review of Scientific Instruments*, 83(3):033504, March 2012.
- [22] T Lafleur, F Cannat, J Jarrige, P Q Elias, and D Packan. Electron dynamics and ion acceleration in expanding-plasma thrusters. *Plasma Sources Science and Technology*, 24(6):065013, November 2015.
- [23] Shae Williams and Ivana Hrbud. RF Cable Heating Effects on a Micronewton-scale Torsional Thrust Stand. In *46th AIAA/ASME/SAE/ASEE Joint Propulsion Conference & Exhibit*, Nashville, TN, July 2010. American Institute of Aeronautics and Astronautics.
- [24] M. Wijnen, J. Navarro-Cavallé, and P. Fajardo. Mechanically Amplified Milli-Newton Thrust Balance for Direct Thrust Measurements of Electric Thrusters for Space Propulsion. *IEEE Transactions on Instrumentation and Measurement*, 70:1–18, 2021. Conference Name: IEEE Transactions on Instrumentation and Measurement.
- [25] Kurt A. Polzin, Thomas E. Markusic, Boris J. Stanojev, Amado DeHoyos, and Benjamin Spaun. Thrust stand for electric propulsion performance evaluation. *Review of Scientific Instruments*, 77(10):105108, October 2006.
- [26] Kyaw Swar, Daniel Staab, Emmanuelle Rosati Azevedo, Alberto Garbayo, Silvia Masillo, James Stubbing, Andrea Fabris, and Rachel Moloney. Electric Propulsion Torsional Thrust Balance with Wireless Microwave Power Transfer. March 2021.
- [27] David M. Pozar. *Microwave engineering*. Wiley, Hoboken, NJ, 4th ed edition, 2012. OCLC: ocn714728044.
- [28] Eric Vigés, Benjamin A Jorns, Alec D. Gallimore, and John Patrick Sheehan. University of Michigan's Upgraded Large Vacuum Test Facility. Vienna, Austria, September 2019.
- [29] S. Correyero, M. Merino, Paul-Quentin Elias, J. Jarrige, D. Packan, and E. Ahedo. Characterization of diamagnetism inside an ECR thruster with a diamagnetic loop. *Physics of Plasmas*, 26(5):053511, May 2019.
- [30] Theo Vialis, Julien Jarrige, and Denis Packan. Geometry optimization and effect of gas propellant in an electron cyclotron resonance plasma thruster. Atlanta, GA, October 2017.
- [31] Benjamin Wachs and Benjamin A Jorns. Background pressure effects on ion dynamics in a low-power magnetic nozzle thruster. *Plasma Sources Science and Technology*, February 2020.
- [32] Simon Peterschmitt and Denis Packan. Impact of the Microwave Coupling Structure on an Electron-Cyclotron Resonance Thruster. *Journal of Propulsion and Power*, pages 1–10, September 2021.
- [33] Christopher M Cretel, Mazzin M Ajamia, Derek S Thompson, and M Umair Siddiqui. Torsional Balance Thrust Measurement Techniques for Small RF Thrusters. page 15, 2019.
- [34] Franz Georg Hey, Andreas Keller, Claus Braxmaier, Martin Tajmar, Ulrich Johann, and Dennis Weise. Development of a Highly Precise Micronewton Thrust Balance. *IEEE Transactions on Plasma Science*, 43(1):234–239, January 2015. Conference Name: IEEE Transactions on Plasma Science.
- [35] Manuel Gamero-Castaño. A torsional balance for the characterization of microNewton thrusters. *Review of Scientific Instruments*, 74(10):4509–4514, October 2003.
- [36] John Ziemer. Performance measurements using a sub-micronewton resolution thrust stand. 2001.



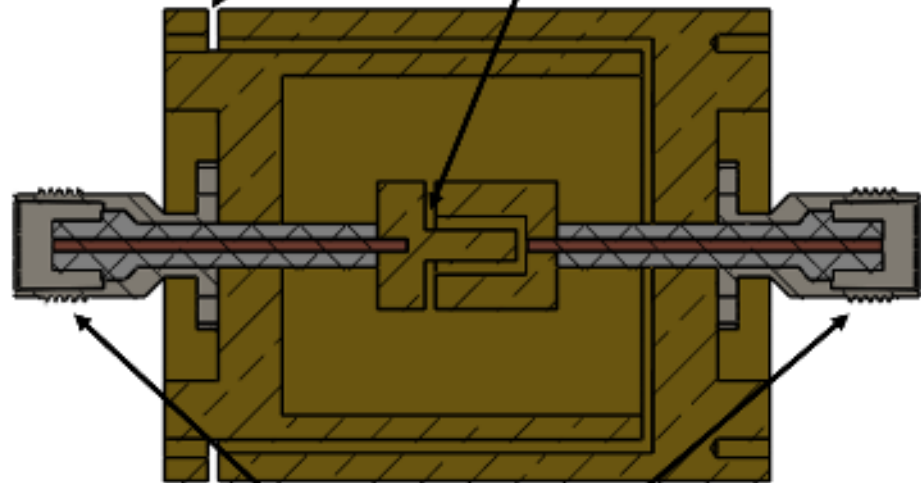




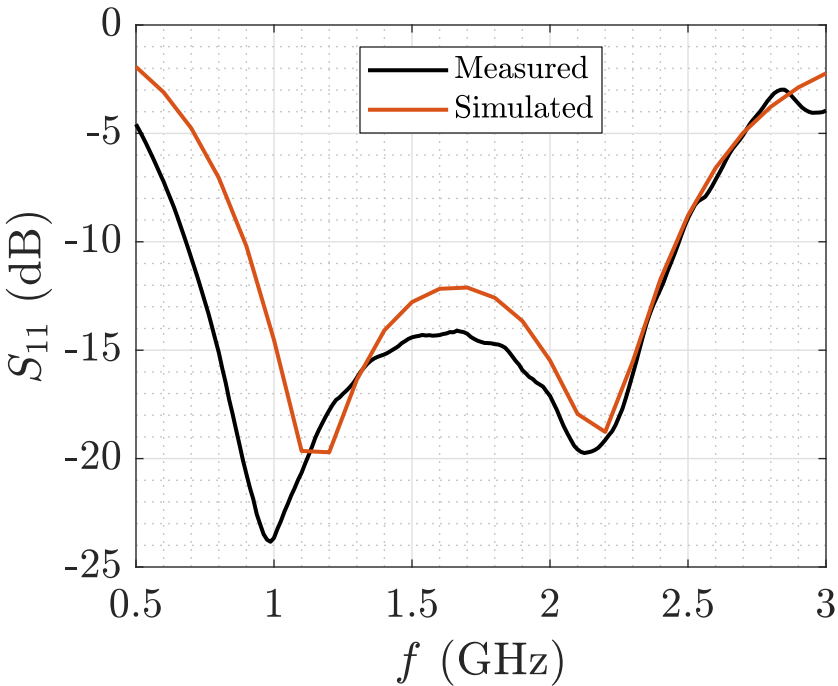


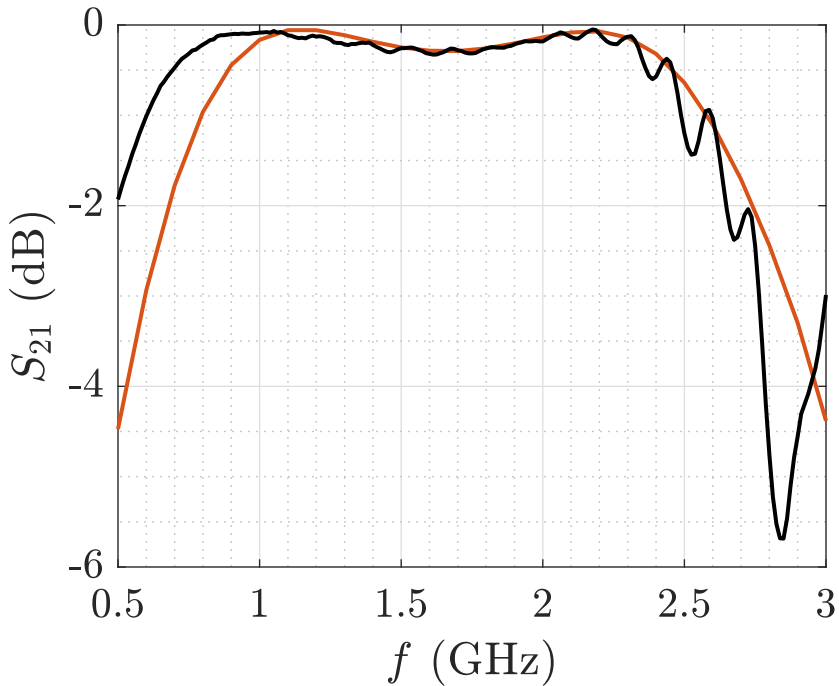
Outer Conductor Gap

Inner Conductor Gap



**TNC
Connectors**







permanent magnets

antenna

coaxial line

propellant injection

magnetic field lines

